Electronic Supplementary Material (ESI) for Chemical Science.
This journal is © The Royal Society of Chemistry 2021

Supporting Information

Helix-mediated over 1 nm-range chirality recognition by ligand-to-ligand interactions of dinuclear helicates

Natsumi Suko, Hideki Itamoto, Yoshinori Okayasu, Naoya Okura, dand Junpei Yuasa*

Experimental Section

General. Chemicals were purchased from FUJIFILM Wako Pure Chemical Corp. and used as received without further purification. (*R*,*R*)- and (*S*,*S*)-2,6-bis(4-isopropyl-2-oxazolin-2-yl)pyridine, (*R*,*R*)- and (*S*,*S*)-2,6-bis(4-phenyl-2-oxazolin-2-yl)pyridine were obtained from Tokyo Chemical Industry Co., Ltd. (TCI). ^{19}F NMR spectra were measured with JEOL JNM-ECZ400S. Mass spectra were measured with mass spectrometers (JEOL JMS-T100CS). The emission and UV-vis absorption spectra were measured at room temperature using JASCO FP-6500 and V-660, respectively. CD spectra were measured by JASCO J-725 Spectrophotometer.

Synthesis. 5,5-bis(4,4,4-trifluoro-1,3-dioxobutyl)(2,20-bithienyl)-1,3-butanedione (L_2), 1,1'-[2,2':5',2''-terthiophene]-5,5''-diylbis[4,4,4-trifluoro-1,3-butanedione (L_3), 1-[2,2'-bithiophen]-5-yl-4,4,4-trifluoro-1,3-butanedione (L_2') were prepared according to a procedure described previously.[1–4] Precursor complexes **2Th**, **3Th**, and **2Th'** were referenced as describe in the literature.[2]

Structure Modeling. The optimized structures of metal complexes were calculated with GAUSSIAN 09.

Synthesis of Precursor Complex 2Th (S1). L_2 (50.8 mg, 0.11 mmol) was dissolved in 50 mL MeOH. $(CH_3COO)_3Eu{\cdot}nH_2O$ (25.3 mg, 0.08 mmol) in 20 mL MeOH was added dropwise to the solution and stirred 1 h at 40 °C. The precipitate formed after the addition of water was filtered and dried under vacuum (39.0 mg, 65.4 %). HRMS [ESI-MS (positive)]: *m*/*z* calcd for $C_{48}H_{18}Eu_2F_{18}NaO_{12}S_6$ $^+$ $[Eu_2(L_2 - 2H)_3 + Na]^+$: 1648.71573; found 1648.71546. ^{1}H NMR (300 MHz, acetone-d_6) δ 8.19 (d, J = 3.8 Hz, 6H), 7.21 (d, J = 3.4 Hz, 6H).

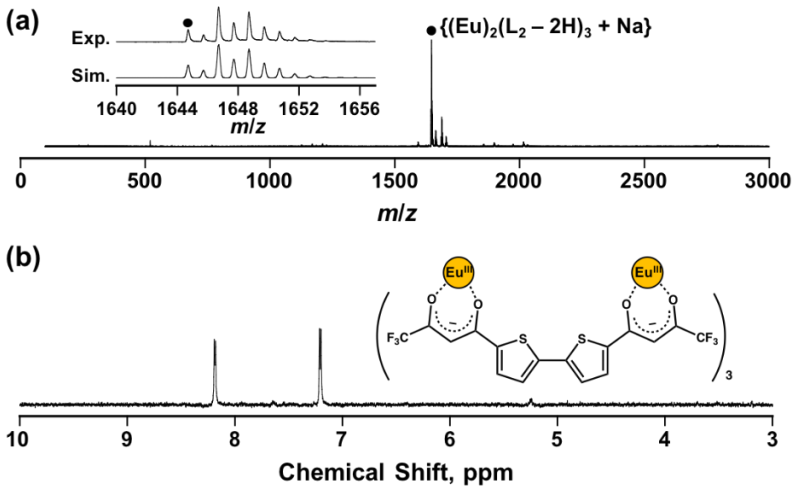

Fig. S1 (a) Positive ESI mass spectrum of **2Th** in acetone. (Inset) Isotopically resolved signal with the calculated isotopic distributions for $\{(Eu)_2(L_2 - 2H)_3 + Na\}$. (b) ^{1}H NMR spectrum of **2Th** in acetone-d_6.

Synthesis of Precursor Complex 3Th (S2). L_3 (190.0 mg, 0.36 mmol) was dissolved in 350 mL MeOH. $(CH_3COO)_3Eu{\cdot}nH_2O$ (80.2 mg, 0.24 mmol) in 60 mL MeOH was added dropwise to the solution and stirred 3 h at 40 °C. The precipitate formed after the addition of water was filtered and dried under vacuum (177 mg, 77.9 %). HRMS [ESI-MS (positive)]: *m*/*z* calcd for $C_{60}H_{24}Eu_2F_{18}NaO_{12}S_9^+$ $[Eu_2(L_3 - 2H)_3 + Na]^+$: 1894.67889; found 1894.67799. ^{1}H NMR (300 MHz, acetone-d_6) δ 8.71 (s, 6H), 7.68 (d, J = 3.4 Hz, 6H), 7.13 (d, J = 4.5 Hz, 6H).

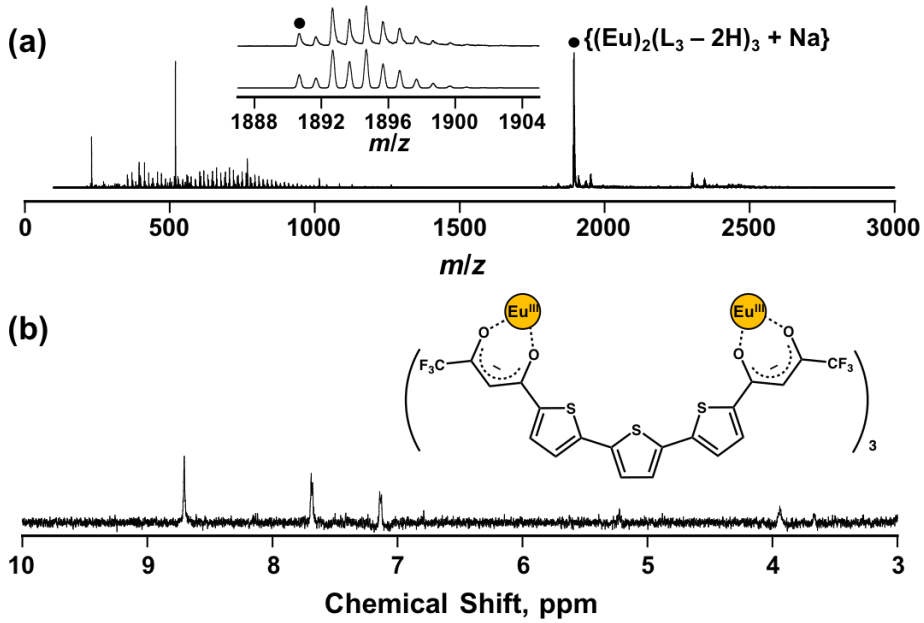

Fig. S2 (a) Positive ESI mass spectrum of **3Th** in acetone. (Inset) Isotopically resolved signal with the calculated isotopic distributions for $\{(Eu)_2(L_3 - 2H)_3 + Na\}$. (b) ^{1}H NMR spectrum of **3Th** in acetone-d_6.

Synthesis of Precursor Complex 2Th' (S3). L_2' (100.0 mg, 0.33 mmol) was dissolved in 30 mL MeOH. $(CH_3COO)_3Eu{\cdot}nH_2O$ (36.6 mg, 0.11 mmol) in 10 mL MeOH was added dropwise to the solution and stirred 2 h at 40 °C. The precipitate formed after the addition of water was filtered and dried under vacuum (103 mg, 87.9 %). HRMS [ESI-MS (positive)]: *m*/*z* calcd for $C_{36}H_{18}EuF_9NaO_6S_6^+$ $[Eu(L_2' - H)_3 + Na]^+$: 1084.83939; found 1084.83862. ^{1}H NMR (400 MHz, acetone-d_6) δ 7.62–7.56 (m, 6H), 7.29 (dd, J = 5.0, 3.7 Hz, 3H), 6.53 (d, J = 3.7 Hz, 3H), 5.45 (d, J = 3.2 Hz, 3H).

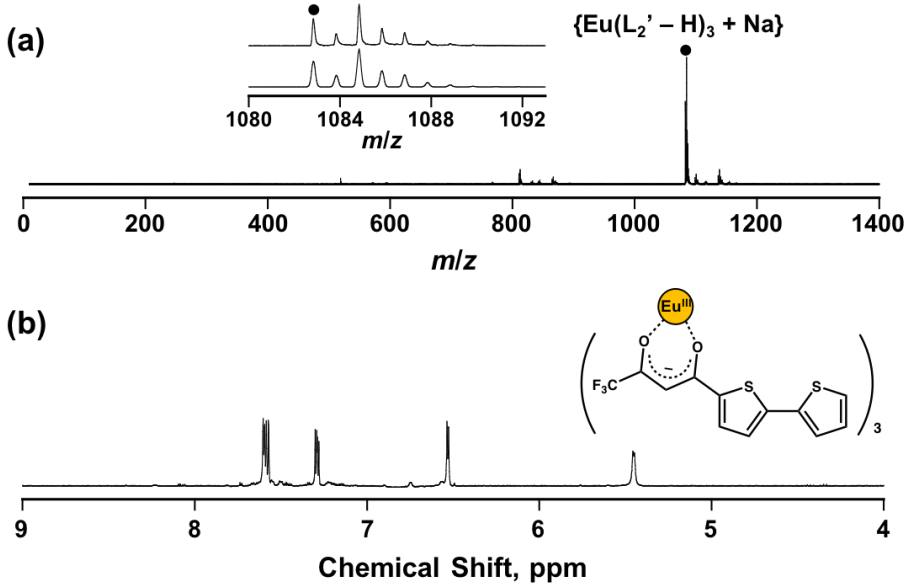

Fig. S3 (a) Positive ESI mass spectrum of **2Th'** in acetone. (Inset) Isotopically resolved signal with the calculated isotopic distributions for $\{Eu(L_2' - H)_3 + Na\}$. (b) ^{1}H NMR spectrum of **2Th'** in acetone-d_6.

Table S1. Comparison between X-ray crystal structure and DFT optimized structures of **2Th**-$L^R \cdot L^R$ in terms of selected atom distance

Structure	$d_{\pi\text{-}\pi}$ [Å] [a]	$d_{\text{Ln-Ln}}$ [Å]
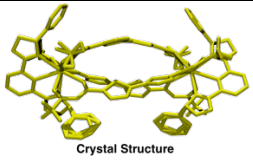 Crystal Structure	3.567, 3.829	12.675
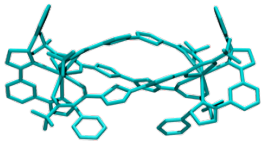 DFT Optimized Structure [CAM-B3LYP/def2SVP (Ligands)/def2TZVPP (La)] *b*	3.820, 4.215	12.528
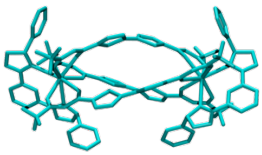 DFT Optimized Structure [BPV86/def2SVP (Ligands)/def2TZVPP (La)] *b*	4.057, 4.320	12.451
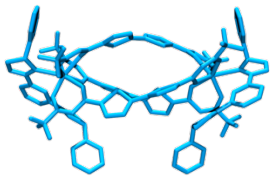 DFT Optimized Structure [DFT/CAM-B3LYP-6-31G(d)/LANL2DZ (Sc)] *c*	4.382, 5.296	12.235

[a]Distance between the phenyl ring of L^R and the diketonate ligand. [b]Eu atoms were replaced by La atoms. [c]Eu atoms were replaced by Sc atoms.

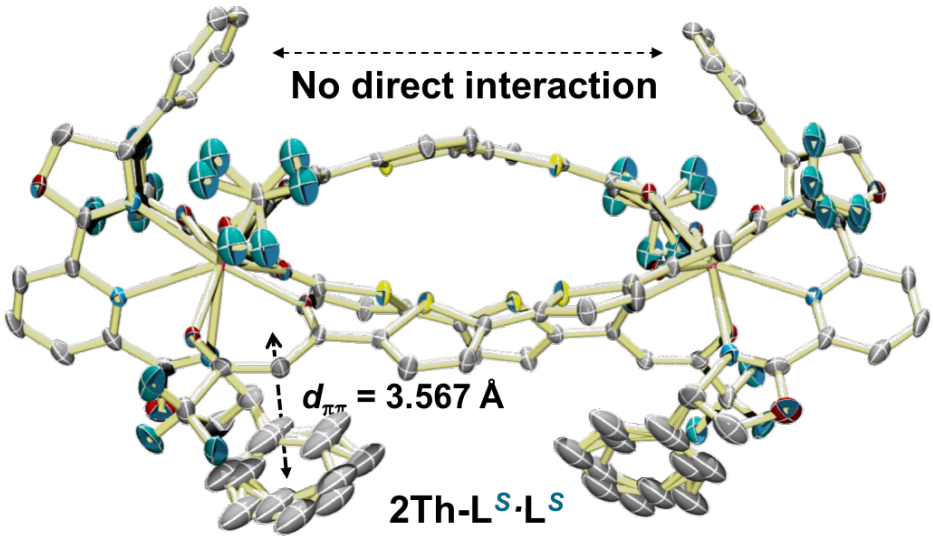

Fig. S4 X-ray crystal structure (ORTEP view, 50% probability) of **2Th**-L^S·L^S (CCDC2036830). Hydrogen atoms are omitted for clarity.

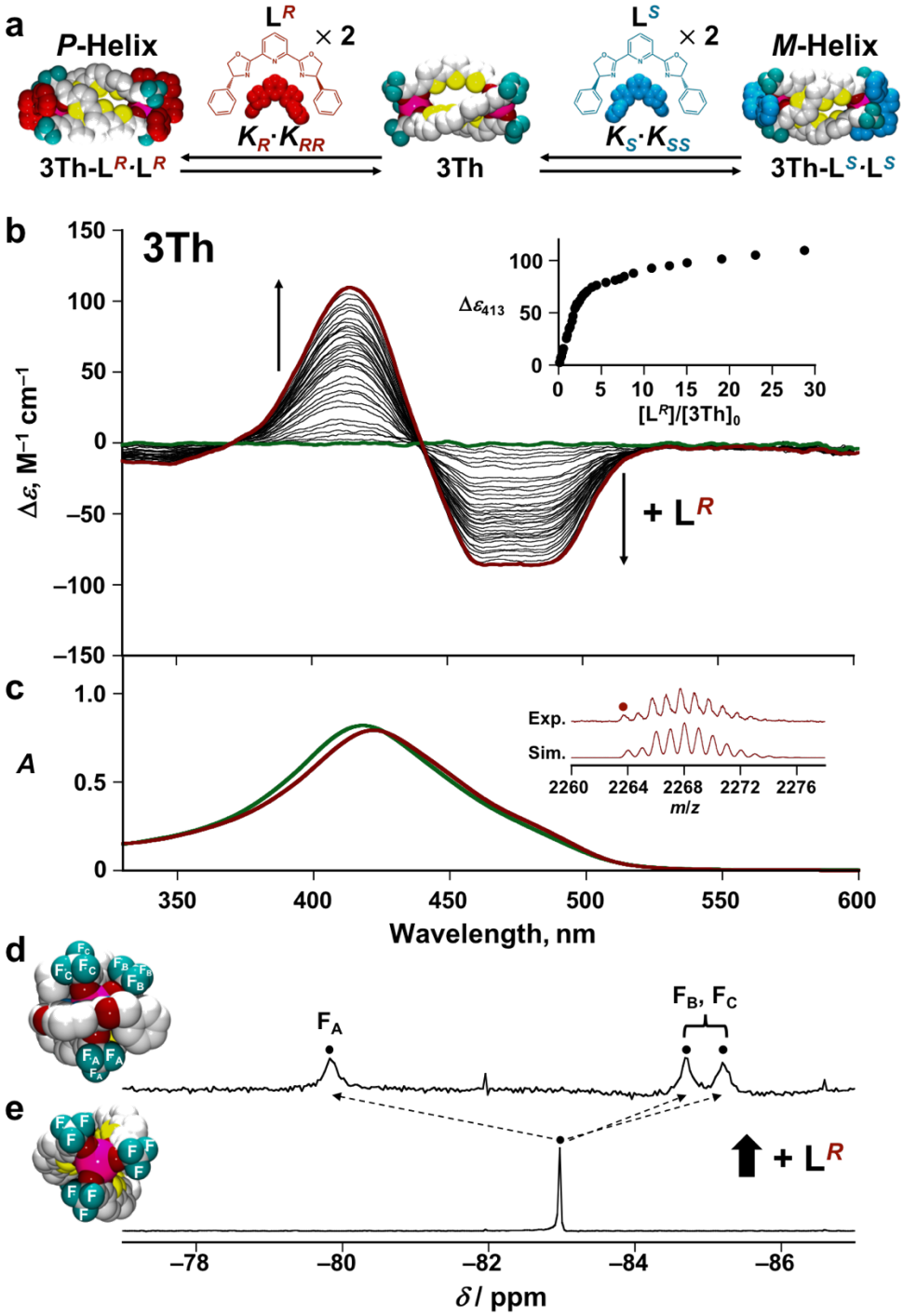

Fig. S5 (a) Self-assembly formation of **3Th** with L^R (left) and that with L^S (right). (b) CD and (c) UV-vis absorption spectra of **3Th** (5.3×10^{-6} M) in the presence of L^R [0 (green line)–1.5×10^{-4} M (red line)] in acetone at 298 K. ^{19}F NMR spectra of **3Th** (e) in the absence and (d) presence of 2 eq of L^R in acetone-d_6 at 298 K. (Insets) (b) Plot of $\Delta\varepsilon$ at 413 nm versus $[L^R]/[\mathbf{3Th}]_0$. (c) Negative ESI mass spectrum of **3Th** in the presence of L^R in acetone with the calculated isotopic distributions for $\{(Eu)_2(L_3 - 2H)_3(L^R)_2 + CH_3COCH_3\}$.

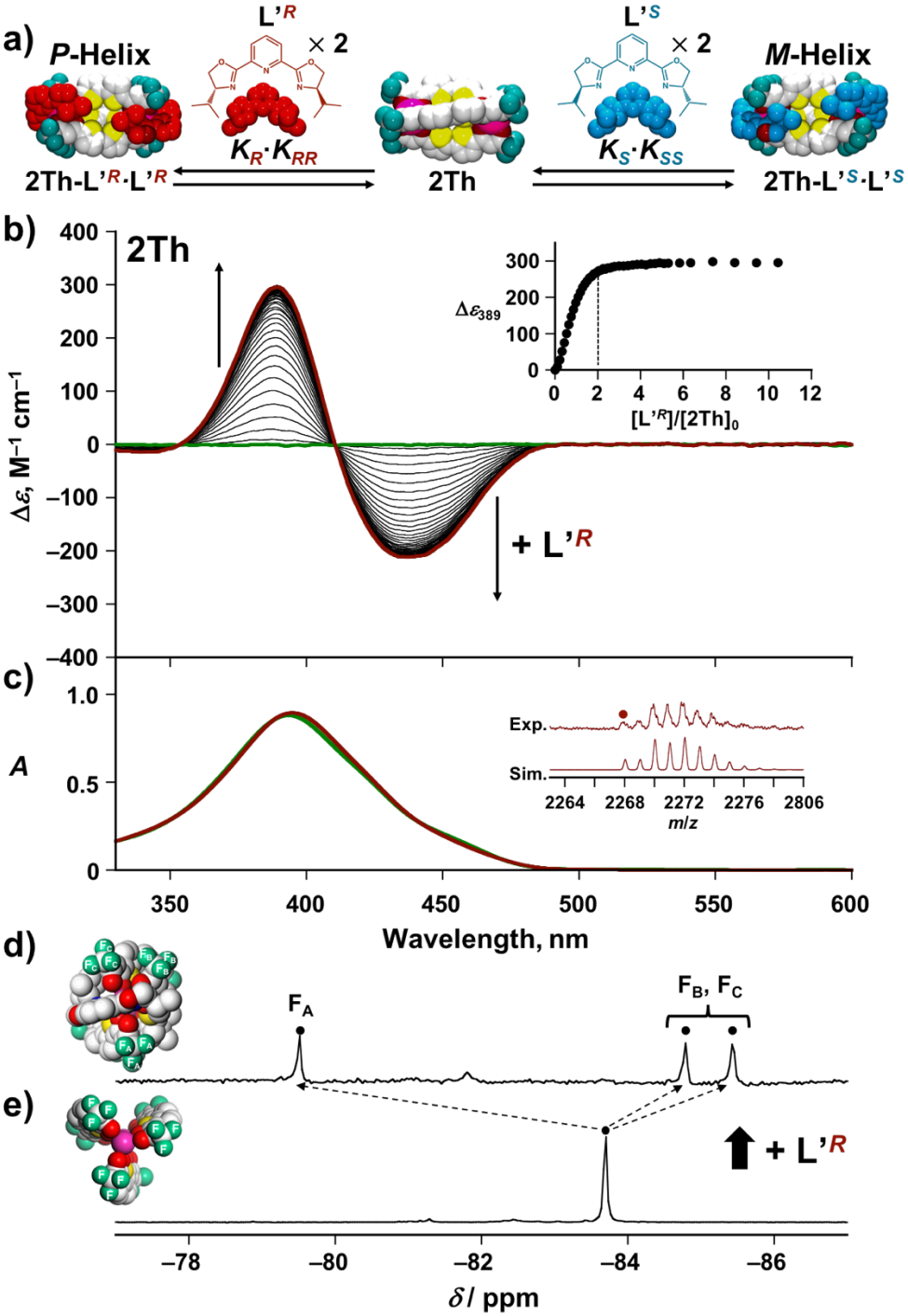

Fig. S6 (a) Self-assembly formation of **2Th** with L'^{R} (left) and that with L'^{S} (right). (b) CD and (c) UV-vis absorption spectra of **2Th** (6.9×10^{-6} M) in the presence of L'^{R} [0 (green line)–7.2×10^{-5} M (red line)] in acetone at 298 K. ^{19}F NMR spectra of **2Th** (e) in the absence and (d) presence of 2 eq of L'^{R} in acetone-d_6 at 298 K. (Insets) (b) Plot of $\Delta\varepsilon$ at 389 nm versus [L'^{R}]/[**2Th**]$_0$. (c) Negative ESI mass spectrum of **2Th** in the presence of L'^{R} in acetone with the calculated isotopic distributions for $\{(Eu)_2(L_2 - 2H)_3(L'^R)_2 + 2Na - 2H\}$.

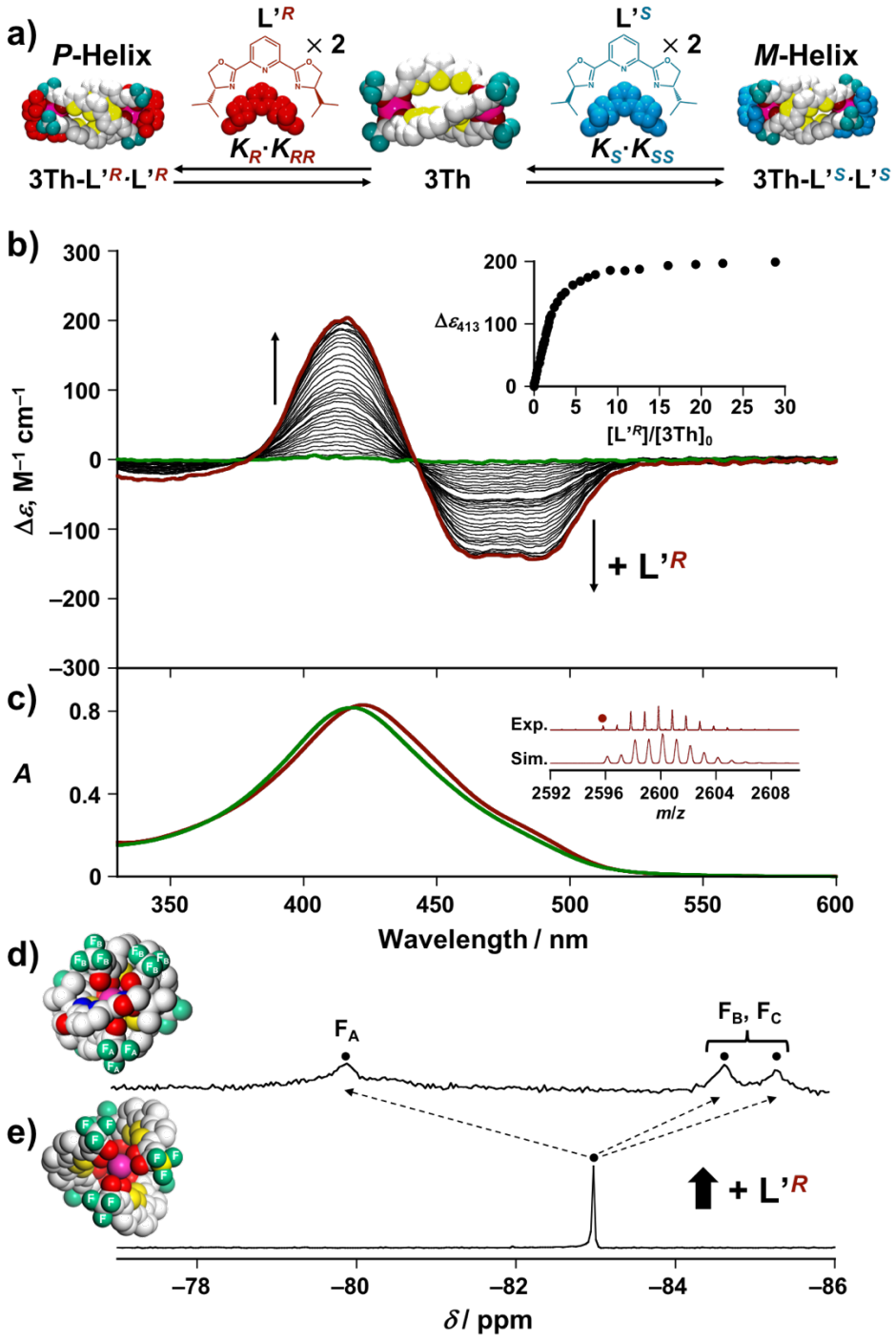

Fig. S7 a) Self-assembly formation of **3Th** with L'^{R} (left) and that with L'^{S} (right). b) CD and c) UV-vis absorption spectra of **3Th** (5.3×10^{-6} M) in the presence of L'^{R} [0 (green line)–1.5×10^{-4} M (red line)] in acetone at 298 K. ^{19}F NMR spectra of **3Th** e) in the absence and d) presence of 2 eq of L'^{R} in acetone-d_6 at 298 K. (Insets) (b) Plot of $\Delta\varepsilon$ at 413 nm versus [L'^{R}]/[**3Th**]$_0$. (c) Negative ESI mass spectrum of **3Th** in the presence of L'^{R} in acetone with the calculated isotopic distributions for $\{(Eu)_2(L_2 - 2H)_3(L'^R)_2 + CH_3COCH_3 + 2H_2O + CH_3OH\}$.

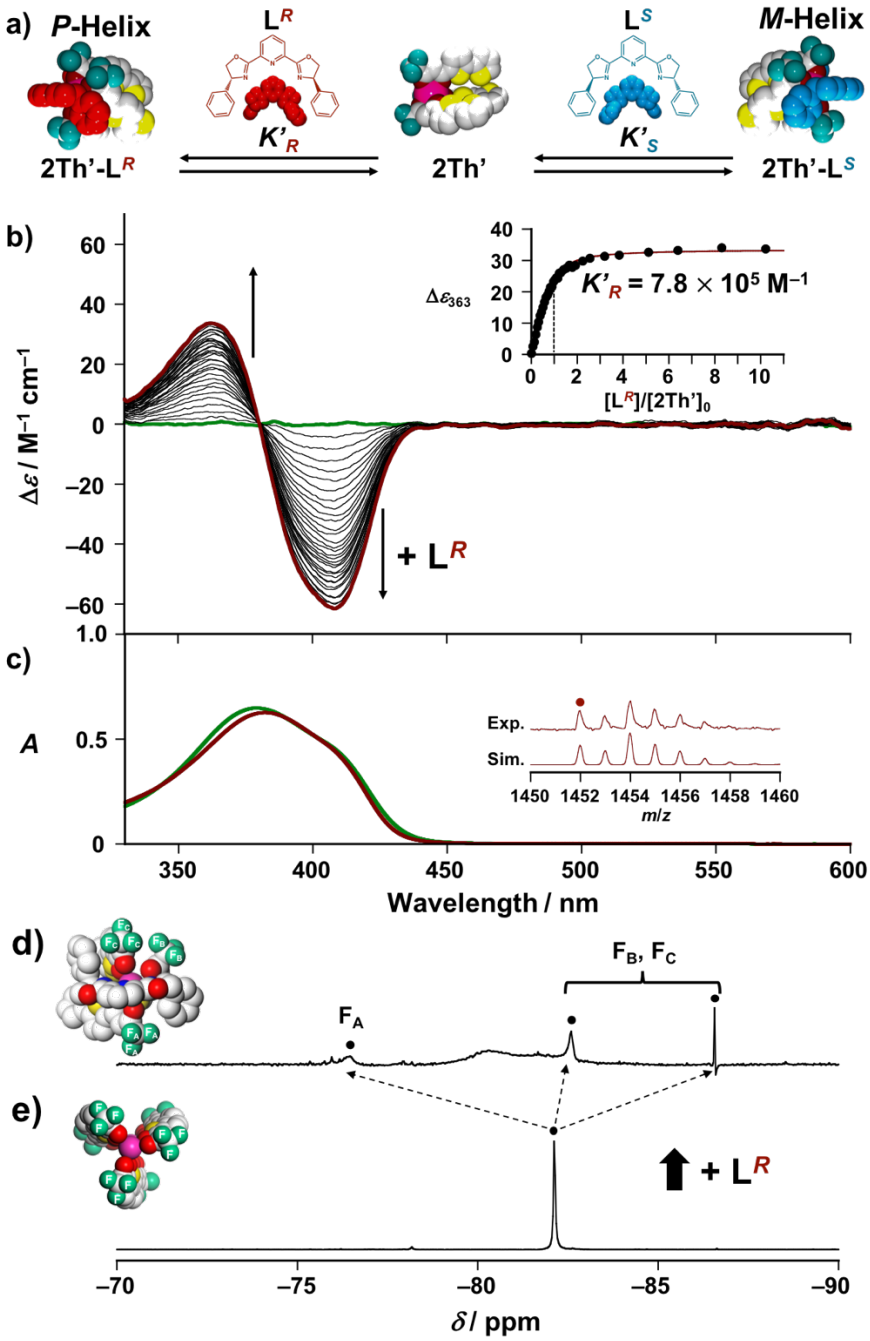

Fig. S8 (a) Self-assembly formation of **2Th'** with L^R (left) and that with L^S (right). (b) CD and (c) UV-vis absorption spectra of **2Th'** (9.6×10^{-6} M) in the presence of L^R [0 (green line)–9.6×10^{-5} M (red line)] in acetone at 298 K. ^{19}F NMR spectra of **2Th'** (d) in the absence and (e) presence of 1 eq of L^R in acetone-d_6 at 298 K. (Insets) (b) Plot of $\Delta\varepsilon$ at 363 nm versus $[L^R]/[\mathbf{2Th'}]_0$. Simulated curve was obtained based on the 1:1 binding model. (c) Positive ESI mass spectrum of **2Th'** in the presence of L^R in acetone with the calculated isotopic distributions for $\{(Eu)_2(L_2' - H)_3(L^R) + Na\}$.

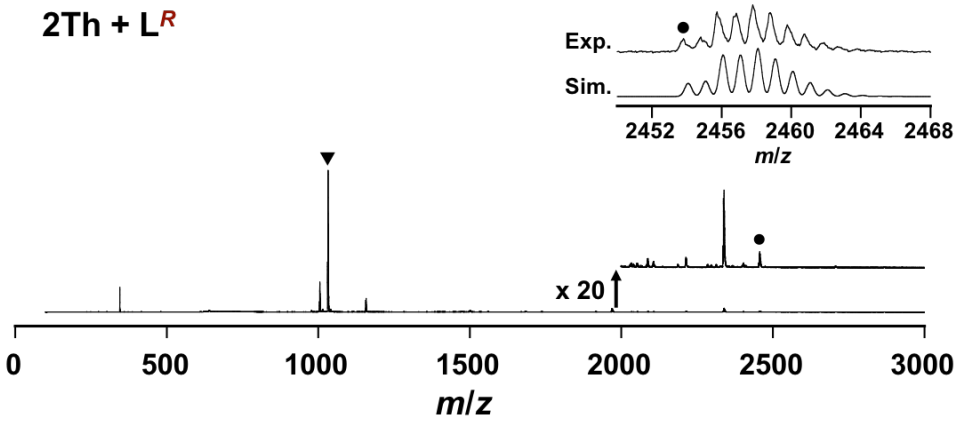

Fig. S9 Negative ESI mass spectrum of **2Th** in the presence of L^R in acetone. (Insets) Mass intensity was vertically expanded in the range *m/z* = 2000–3000. Isotopically resolved signals with the calculated isotopic distributions for $\{(Eu)_2(L_2 - 2H)_3(L^R)_2 + CH_3COCH_3 + 2H_2O\}$. Mass peak anted by triangle corresponds to the mono-coordinated species (**2Th**-L^R), which probably arises from fragmentation of di-coordinated species (**2Th**-L^R·L^R).

Time-dependent DFT studies (S10-12). Initially, we calculated DFT optimized structures of the 1D helicate lanthanide assemblies by replacing the Eu atoms with La atoms to reduce the calculation complexity. The resulting DFT optimized structure of **2Th**-L^S·L^S showed good agreement with that of the crystal structure (Figure S10a). Conversely, time-dependent (TD) DFT with using the resulting DFT optimized structures could not be accomplished due to an error with regard to frozen core potential of La atoms. Hence, we also calculated the DFT optimized structures by replacing the Eu atoms with Sc atoms. Although the resulting DFT optimized structure of **2Th**-L^S·L^S exhibited differences with the crystal in terms of the positions of the chiral guest co-ligands (L^S), the helix structure of the mediator unit was still preserved (Figure S10b). Then, TD-DFT calculations of 1D helicate lanthanide assemblies were performed with using the DFT optimized structures comprising Sc atoms, where the theoretical UV-vis and CD spectra well reproduce the experimentally obtained spectra (Figure S11, and 12).

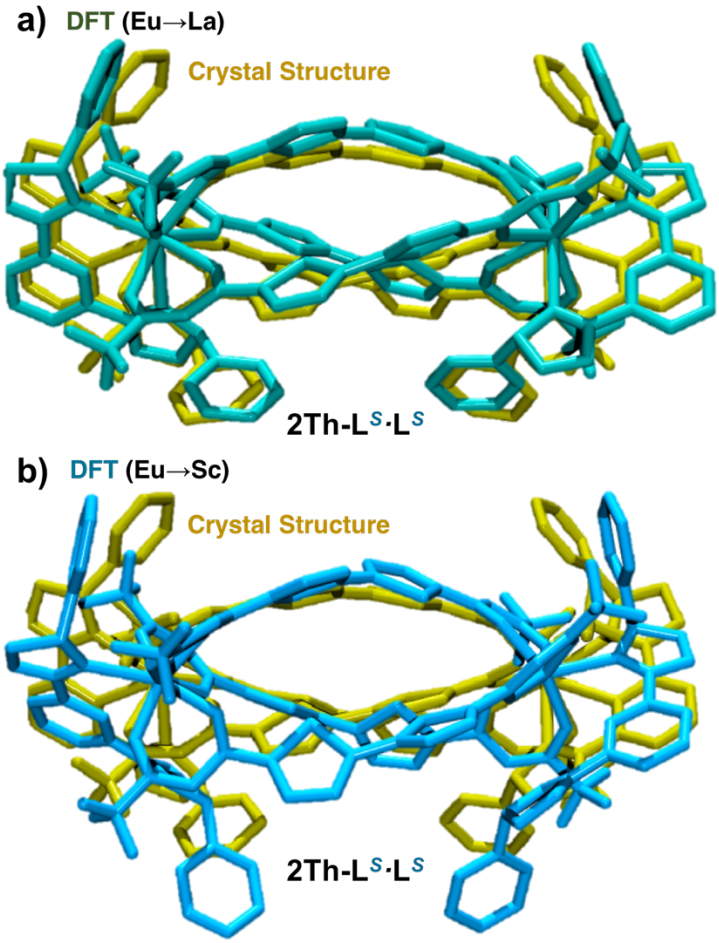

Fig. S10 Overlapping image of X-ray crystal structure (yellow) of **2Th**-L^S·L^S and (a) optimized structure (green) [DFT/CAM-B3LYP/def2SVP (C H N O S F)/def2TZVPP (La)] of **2Th**-L^S·L^S, where the Eu atoms were replaced by La atoms, (b) and the optimized structure (blue) [DFT/CAM-B3LYP-6-31G(d) [C H N O S F]/LANL2DZ (Sc)] of **2Th**-L^S·L^S, where the Eu atoms were replaced by Sc atoms. Hydrogen atoms are omitted for clarity. One of the disordered structures was shown for clarity.

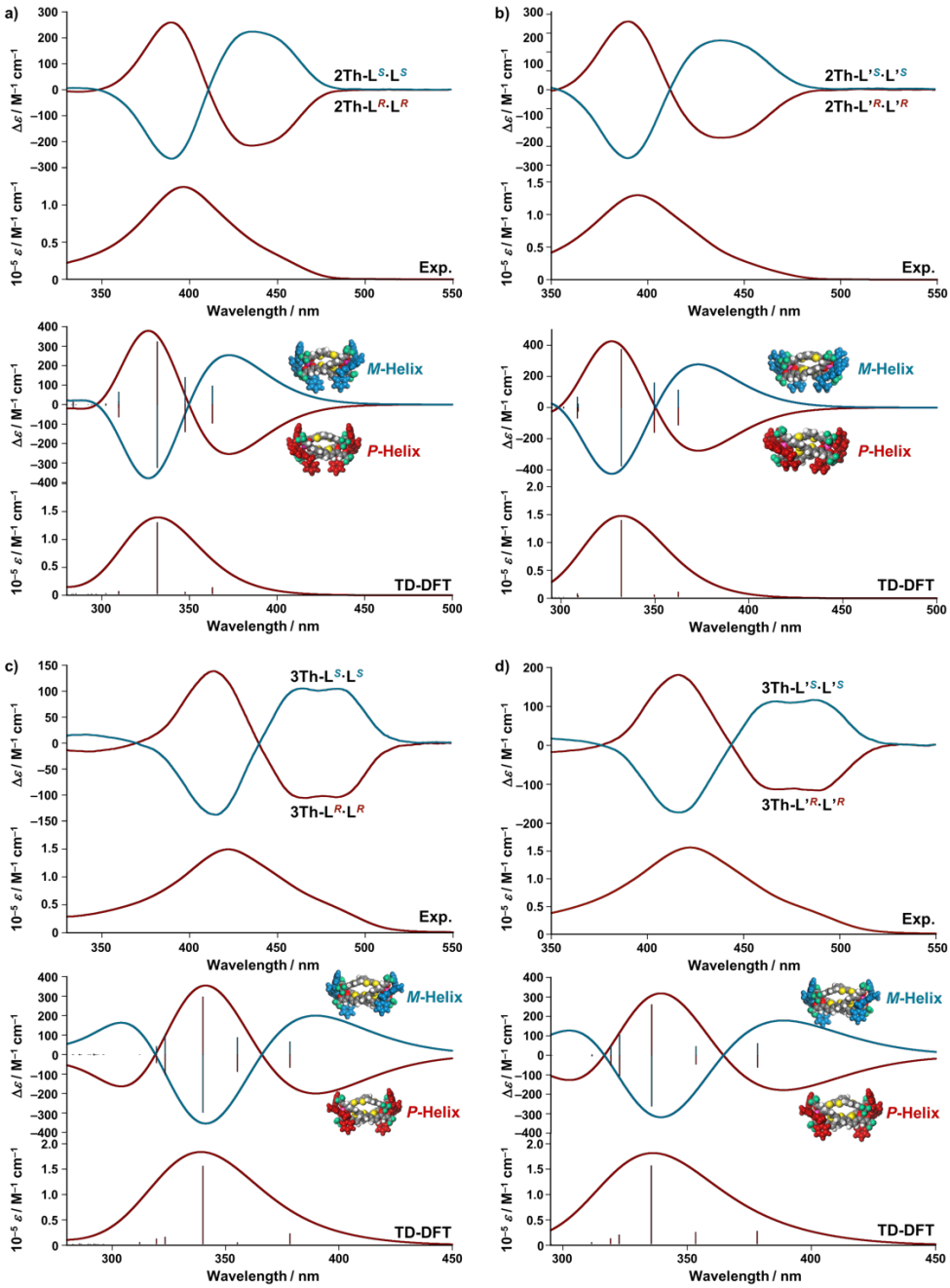

Fig. S11 Experimentally obtained UV-vis and CD spectra of (a) **2Th**-L^R·L^R (red line) and **2Th**-L^S·L^S (blue line), (b) **3Th**-L^R·L^R (red line) and **3Th**-L^S·L^S (blue line), (c) **2Th**-L'^{R}·L'^{R} (red line) and **2Th**-L'^{S}·L'^{S} (blue line), (d) **3Th**-L'^{R}·L'^{R} (red line) and **3Th**-L'^{S}·L'^{S} (blue line) in acetone. Theoretical CD spectra [time dependent-DFT/CAM-B3LYP-6-31G(d) [C H N O S F]/LANL2DZ (Sc)] of the optimized structure [DFT/ CAM-B3LYP-6-31G(d) [C H N O S F]/LANL2DZ (Sc)] of a) *P*-**2Th**-L^R·L^R (red line) and *M*-**2Th**-L^S·L^S (blue line), b) *P*-**3Th**-L^R·L^R (red line) and *M*-**3Th**-L^S·L^S (blue line), (c) *P*-**2Th**-L'^{R}·L'^{R} (red line) and *M*-**2Th**-L'^{S}·L'^{S} (blue line), (d) *P*-**3Th**-L'^{R}·L'^{R} (red line) and *M*-**3Th**-L'^{S}·L'^{S} (blue line), where the Eu atoms were replaced by Sc atoms to reduce the calculation complexity.

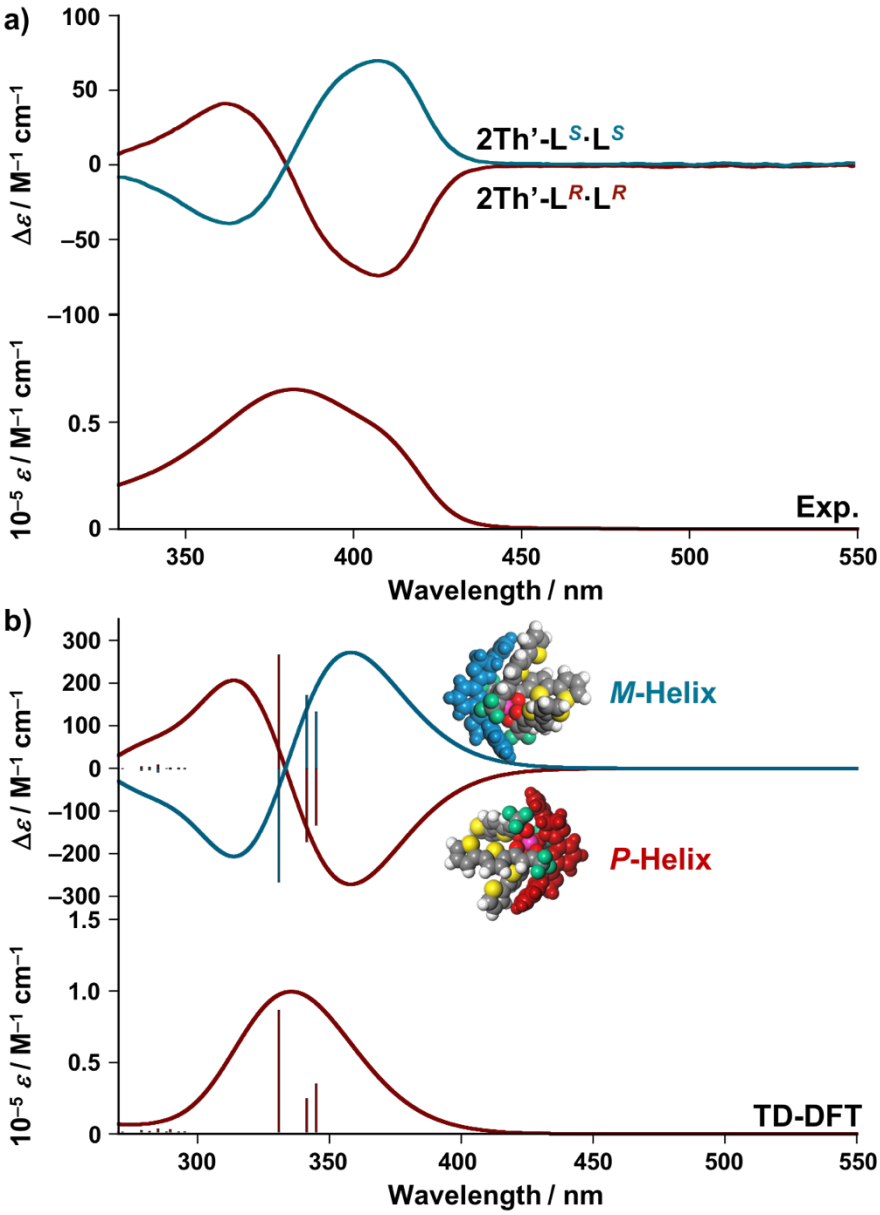

Fig. S12 (a) Experimentally obtained UV-vis and CD spectra of **2Th'**-$L^R{\cdot}L^R$ (red line) and **2Th'**-$L^S{\cdot}L^S$ in acetone. (b) Theoretical CD spectra [time dependent-DFT/CAM-B3LYP-6-31G(d)/LANL2DZ (Sc)] of the optimized structure [DFT/ CAM-B3LYP-6-31G(d) [C H N O S F]/LANL2DZ (Sc)] of *P*-**2Th'**-$L^R{\cdot}L^R$ (red line) and *M*-**2Th'**-$L^S{\cdot}L^S$ (blue line), where the Eu atoms were replaced by Sc atoms to reduce the calculation complexity.

DFT Studies on 3Th assemblies (S13-S14). DFT study indicates that the two effective $\pi\pi$ stacking interactions observed in *M*-**3Th**-L^{S}·L^{S} are completely lost for that of *P*-isomer (*P*-**3Th**-L^{S}·L^{S}). Similarly, one of the two effective CH–F interactions found in *M*-**3Th**-L'^{S}·L'^{S} is lost for *P*-**3Th**-L'^{S}·L'^{S}. It should be noted that number of atoms of the **3Th**-assemblies is too large to perform frequency calculation required for the zero point energy correction, and therefore the energy estimation of the assemblies of the **3Th**-assemblies could not be accomplished with DFT in this study. However, the reduced number of ligand-to-ligand interaction should have the *P*-isomers (*P*-**3Th**-L^{S}·L^{S} and *P*-**3Th**-L'^{S}·L'^{S}) energetically higher than those of *M*-isomers (*M*-**3Th**-L^{S}·L^{S} and *M*-**3Th**-L'^{S}·L'^{S}).

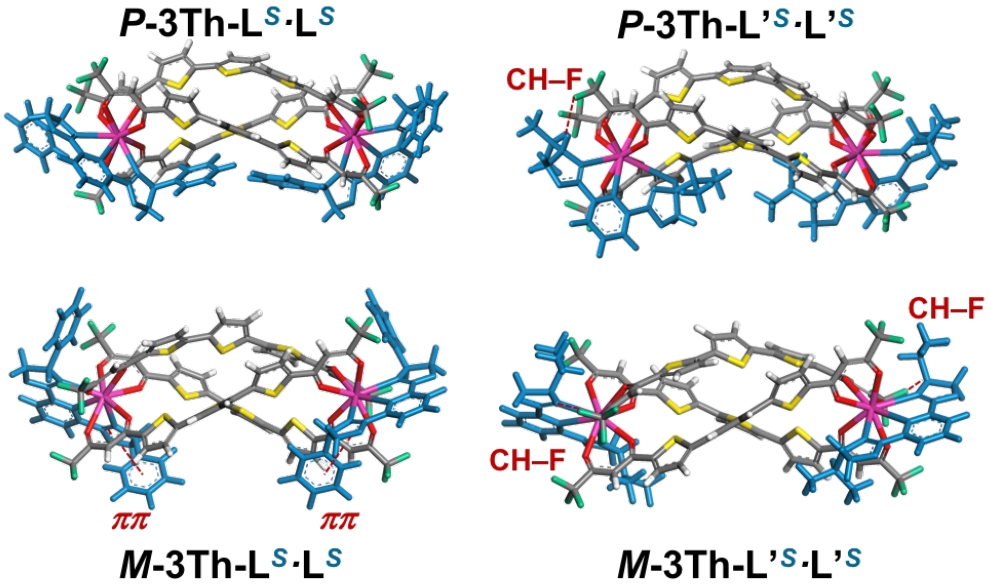

Fig. S13 Optimized structures of *M*-**3Th**-L^{S}·L^{S} and *P*-**3Th**-L^{S}·L^{S}, *M*-**3Th**-L'^{S}·L'^{S} and *P*-**3Th**-L'^{R}·L'^{S} [DFT/CAM-B3LYP/def2SVP (C H N O S F)/def2TZVPP (La)], where the Eu atoms were replaced by La atoms. Red dashed lines show ligand-to-ligand interactions between the chiral co-ligands and the β-diketonate ligands.

The linear relationship $\Delta\varepsilon$ between *ee* observed in the CD experiment of **3Th** with L$^{(R \text{ or } S)}$ (Figure 6b) suggested that the homochiral **3Th**-L^{S}·L^{S} assembly is energetically similar to heterochiral **3Th**-L^{R}·L^{S}. DFT optimized structure of **3Th**-L^{S}·L^{S} indicates two effective $\pi\pi$ stacking interactions between the phenyl rings of L^{S} ligands and the β-diketonate planes. Conversely, two effective $\pi\pi$ stacking interactions are preserved even in heterochiral **3Th**-L^{R}·L^{S}. Hence, no significant energy difference could be expected between **3Th**-L^{S}·L^{S} and **3Th**-L^{R}·L^{S}. Similarly, both homochiral **3Th**-L'^{S}·L'^{S} and heterochiral **3Th**-L'^{R}·L'^{S} assemblies have two effective CH–F interactions inside their assemblies (Figure S14). Noteworthy, the energy

estimation of the assemblies of **3Th** with $L^{(R \text{ or } S)}$ could not be accomplished with DFT, since their number of atoms is too large to perform frequency calculation required for the zero point energy correction.

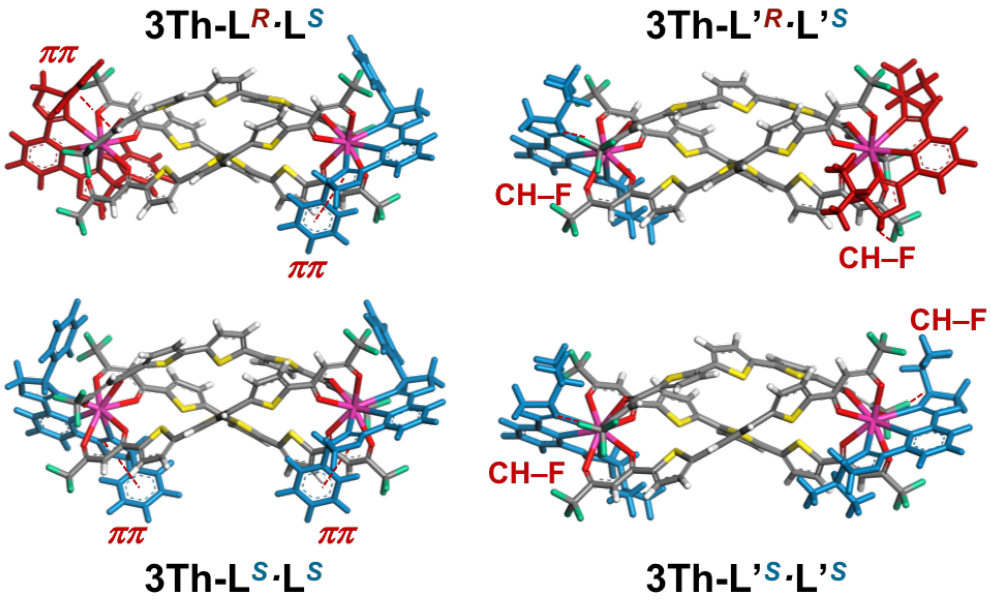

Fig. S14 Optimized structures of **3Th**-$L^S{\cdot}L^S$ and **3Th**-$L^R{\cdot}L^S$, **3Th**-$L'^S{\cdot}L'^S$ and **3Th**-$L'^R{\cdot}L'^S$ [DFT/CAM-B3LYP/def2SVP (C H N O S F)/def2TZVPP (La)], where the Eu atoms were replaced by La atoms. Red dashed lines show ligand-to-ligand interactions between the chiral co-ligands and the β-diketonate ligands.

Appendix : 1 Derivation of Eq (1).

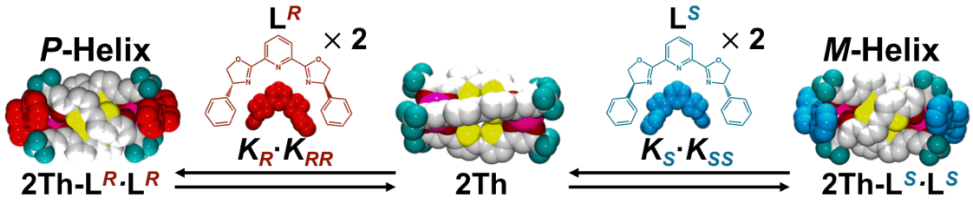

K_R = [**2Th**-L^R]/([**2Th**][L^R]) -------(1) K_S = [**2Th**-L^S]/([**2Th**][L^S]) -------(2)

K_{RR} = [**2Th**-L^R·L^R]/([**2Th**-L^R][L^R]) -------(3) K_{SS} = [**2Th**-L^S·L^S]/([**2Th**-L^S][L^S]) -------(4)

K_{RS} = [**2Th**-L^R·L^S]/([**2Th**-L^R][L^S]) -------(5) K_{SR} = [**2Th**-L^S·L^R]/([**2Th**-L^S][L^R]) -------(6)

$[\mathbf{2Th}]_0$ = [**2Th**-L^R·L^R] + [**2Th**-L^S·L^S] + [**2Th**-L^R·L^S] + [**2Th**-L^S·L^R]-------(7)

ee = ([L^R] – [L^S])/([L^R] + [L^S]) -------(8)

From eq (8) [L^S]/[L^R] = (1 – ee)/(1 + ee) -------(9)

Since [**2Th**-L^R·L^S] = [**2Th**-L^S·L^R], eq (7) should be

$[\mathbf{2Th}]_0$ = [**2Th**-L^R·L^R] + [**2Th**-L^S·L^S] + 2[**2Th**-L^R·L^S] -------(7')

From eq (1) × (3) K_R·K_{RR} = [**2Th**-L^R·L^R]/([**2Th**][L^R]^2) -------(10)

From eq (1) × (5) K_R·K_{RS} = [**2Th**-L^R·L^S]/([**2Th**][L^R][L^S]) -------(11)

From eq (2) × (4) K_S·K_{SS} = [**2Th**-L^S·L^S]/([**2Th**][L^S]^2) -------(12)

From eq (10)/(12) since K_R·K_{RR} = K_S·K_{SS}, 1 = ([**2Th**-L^R·L^R]/[**2Th**-L^S·L^S])([L^S]^2/[L^R]^2)

Then, [**2Th**-L^S·L^S] = [**2Th**-L^R·L^R]([L^S]^2/[L^R]^2) -------(13)

From eq (13) and (7') $[\mathbf{2Th}]_0$ = [**2Th**-L^R·L^R](1 + [L^S]^2/[L^R]^2) + 2[**2Th**-L^R·L^S] -----(14)

From eq (10)/(11) K_{RR}/K_{RS} = ([**2Th**-L^R·L^R]/[**2Th**-L^R·L^S])([L^S]/[L^R])

Then, [**2Th**-L^R·L^S] = [**2Th**-L^R·L^R]([L^S]/[L^R])(K_{RS}/K_{RR}) -------(15)

From eq (14) and (15)

$[\mathbf{2Th}]_0$ = [**2Th**-L^R·L^R](1 + [L^S]^2/[L^R]^2 + ([L^S]/[L^R])(2K_{RS}/K_{RR}))

Then, [**2Th**-L^R·L^R]/$[\mathbf{2Th}]_0$ = 1/(1 + [L^S]^2/[L^R]^2 + ([L^S]/[L^R])(2K_{RS}/K_{RR}))

Then, [**2Th**-L^R·L^R]/$[\mathbf{2Th}]_0$ = (K_{RR}/K_{RS})(1 + ee)^2/(2(K_{RR}/K_{RS})(1 + ee^2) + 2(1 – ee^2)) -------(16)

From eq (13) and (16)

[**2Th**-L^S·L^S]/$[\mathbf{2Th}]_0$ = (K_{RR}/K_{RS})(1 – ee)^2/(2(K_{RR}/K_{RS})(1 + ee^2) + 2(1 – ee^2)) -------(17)

Thus from eq (16) – (17)

([**2Th**-L^R·L^R] – [**2Th**-L^S·L^S])/$[\mathbf{2Th}]_0$ = 2ee(K_{RR}/K_{RS})/((K_{RR}/K_{RS})(1 + ee^2) + 1 – ee^2)--(18)

Since $K_{(hetero)}$ = K_{RS} + K_{SR} = 2K_{RS} = 2K_{SR}.

([**2Th**-L^R·L^R] – [**2Th**-L^S·L^S])/$[\mathbf{2Th}]_0$ = 4ee($K_{RR}/K_{(hetero)}$)/(2($K_{RR}/K_{(hetero)}$)(1 + ee^2) + 1 – ee^2)--(19)

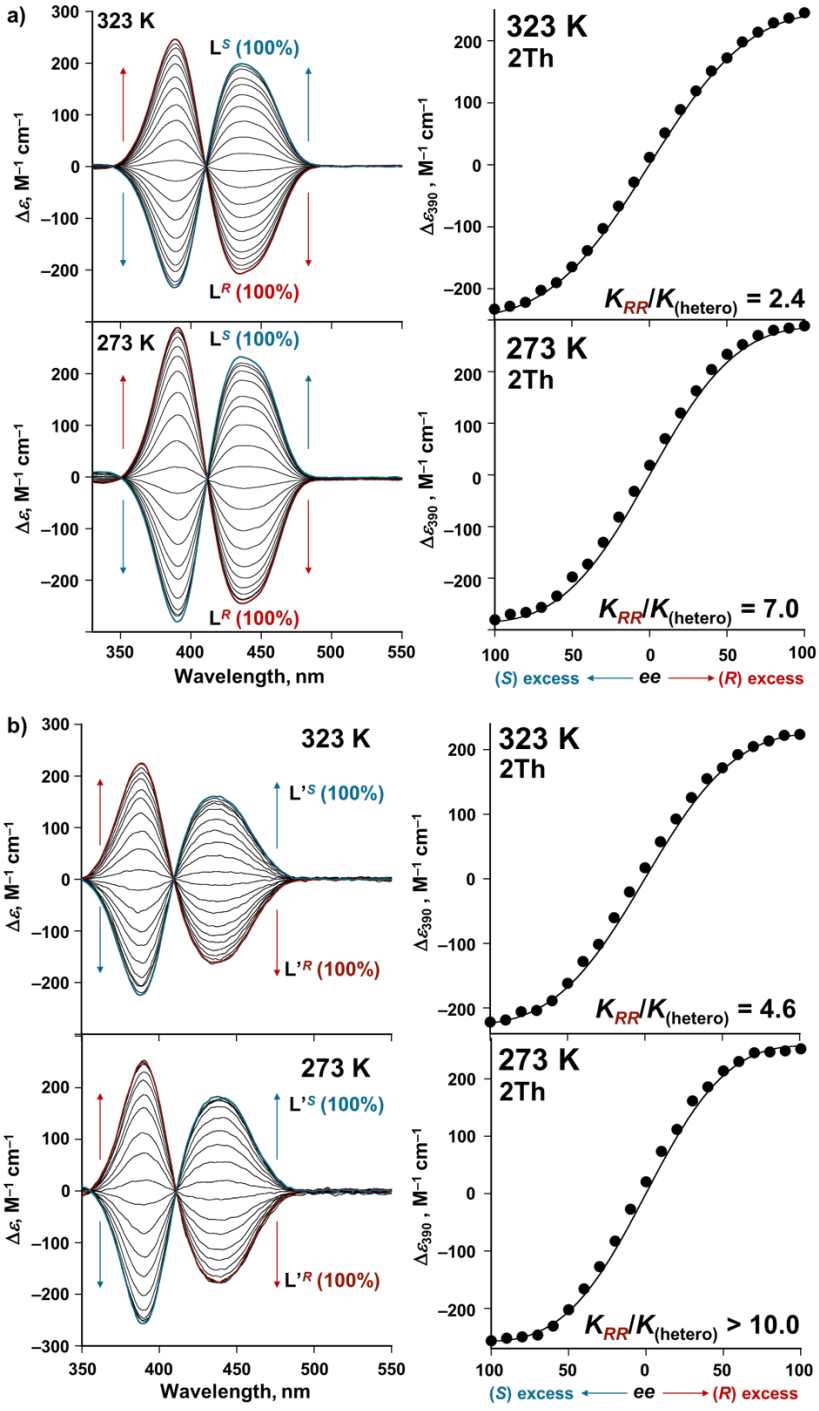

Fig. S15 Left: CD spectra of a) **2Th** (7.2×10^{-6} M) in the presence of different enantiomeric excess (*ee*) of (a) $L^{(R \text{ or } S)}$ (total concentrations: 6.6×10^{-4} M), (b) $L'^{(R \text{ or } S)}$ (total concentrations: 7.5×10^{-4} M) in acetone at 323 K and 273 K. Enantiomeric pure L^R or L'^R (red line); L^S or L'^S (blue line). Right: Plots of $\Delta\varepsilon$ vs *ee* of (a) $L^{(R \text{ or } S)}$ and (b) $L'^{(R \text{ or } S)}$. $K_{(hetero)} = K_{RS} + K_{SR} = 2K_{RS} = 2K_{SR}$.

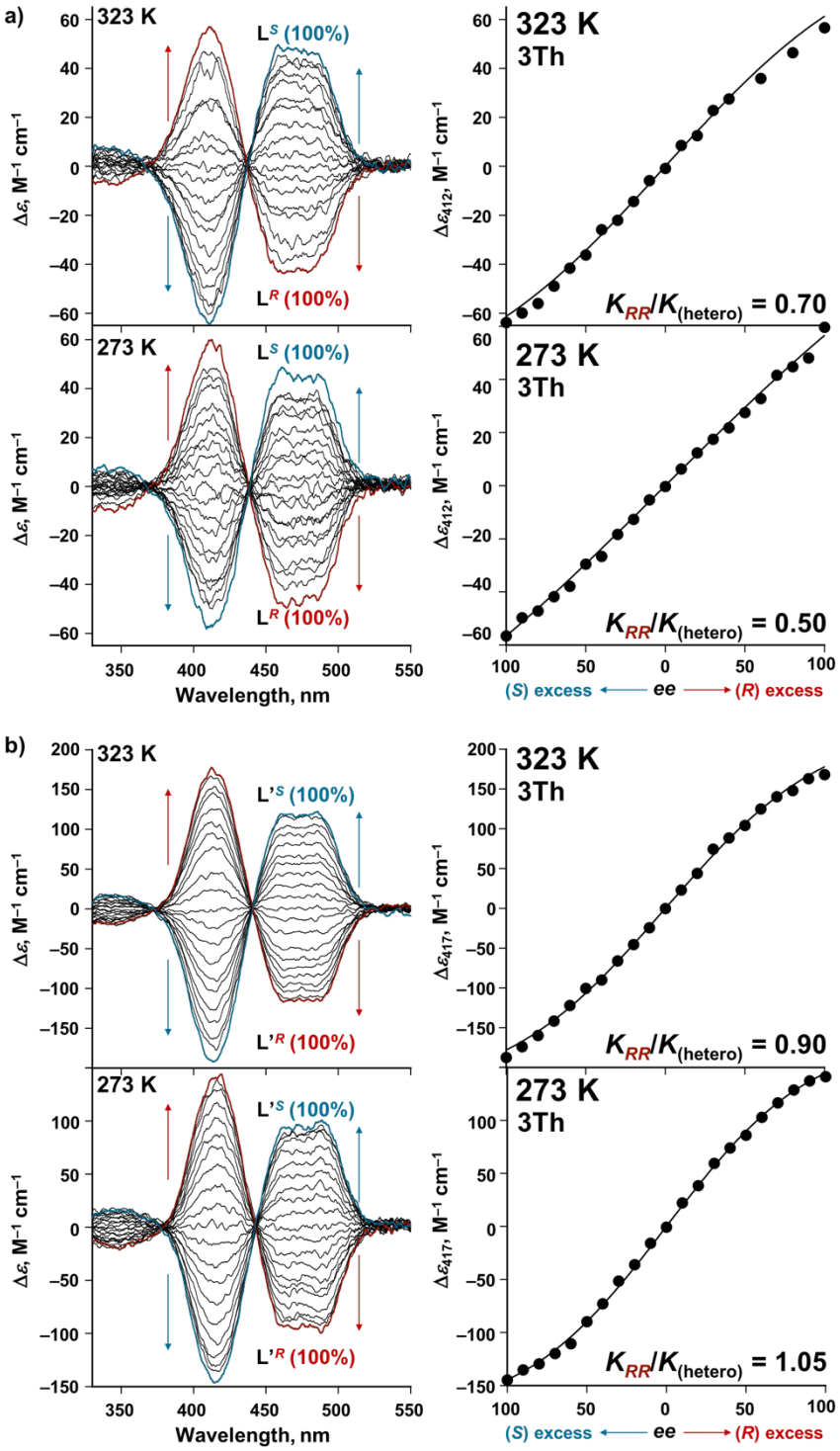

Fig. S16 Left: CD spectra of **3Th** (5.3×10^{-6} M) in the presence of different enantiomeric excess (*ee*) of (a) $L^{(R \text{ or } S)}$ (total concentrations: 4.9×10^{-4} M), (b) $L'^{(R \text{ or } S)}$ (total concentrations: 5.1×10^{-4} M) in acetone at 323 K and 273 K. Enantiomeric pure L^R or L'^R (red line); L^S or L'^S (blue line). Right: Plots of $\Delta\varepsilon$ vs *ee* of (a) $L^{(R \text{ or } S)}$ and (b) $L'^{(R \text{ or } S)}$. $K_{(\text{hetero})} = K_{RS} + K_{SR} = 2K_{RS} = 2K_{SR}$.

With regard to other diamagnetic complexes. Initially, we planned to use the Y^{III} or La^{III} ions (diamagnetic cations) instead of the Eu^{III} ions (paramagnetic cations) to gain access to easier ^1H NMR characterization. During the course of our study, however, we realized that the diamagnetic complexes with the L_3 ligand (having the three thiophene units) have no sufficient solubility to perform our experimental study, while that of the Eu^{III} complex (**3Th**) has a moderate solubility. The diamagnetic complex of L_2 with the Y^{III} ions (**2Th^{Y}**) was prepared by the same procedure as employed for **2Th**: L_2 (200 mg, 0.45 mmol) was dissolved in 200 mL MeOH. $(CH_3COO)_3Y{\cdot}nH_2O$ (81 mg, 0.30 mmol) in 10 mL MeOH was added dropwise to the solution and stirred 2 h at r.t.. The precipitate formed after the addition of water was filtered and dried under vacuum (156 mg, 69.0 %). HRMS [ESI-MS (negative)]: *m/z* calcd. for $C_{48}H_{17}F_{18}O_{12}S_6Y_2$: 1496.68738; found 1496.68701. ^1H NMR (400 MHz, acetone-d_6) δ 7.89 (d, J = 3.7 Hz, 6H), 7.30 (d, J = 3.7 Hz, 6H), 6.48 (s, 6H).

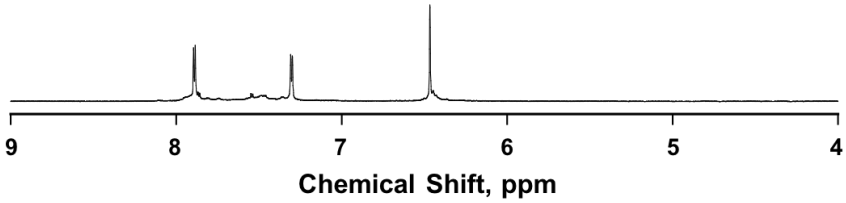

Fig. S17 ^1H NMR spectrum of **2Th^{Y}** in acetone-d_6.

Although ^1H NMR spectra of **2Th^{Y}** undergo line broadening in the presence of the chiral guest co-ligands (probably due to rapid exchange between the bound and free guest co-ligands on ^1H NMR time scale), the resulting NMR spectra obtained under racemic ([L^R]:[L^S] = 1:1) and enantiopure conditions ([L^R]:[L^S] = 2:0) are almost identical (Fig. S20), indicating the predominant formation of the homochiral assemblies (**2Th^{Y}**-$L^R{\cdot}L^R$ and **2Th^{Y}**-$L^S{\cdot}L^S$) under the both conditions. Hence, the ^1H NMR characterization also supports the chiral self-sorting behavior of the shorter helicate **2Th** (and **2Th^{Y}**) and the chiral guest co-ligands.

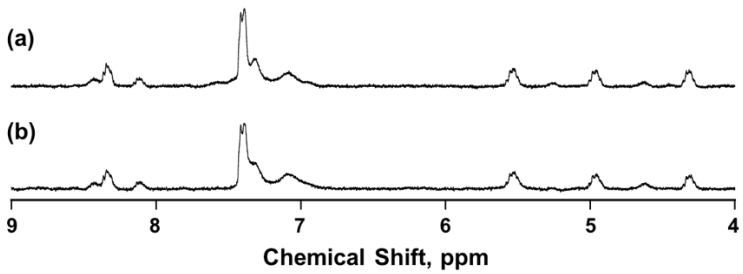

Fig. S18 ^1H NMR spectra of **2Th^{Y}** under the (a) racemic conditions [**2Th^{Y}**]:[L^R]:[L^S] = 1:1:1, (b) enantiopure conditions [**2Th^{Y}**]:[L^R]:[L^S] = 1:2:0 in acetone-d_6 at 298 K.

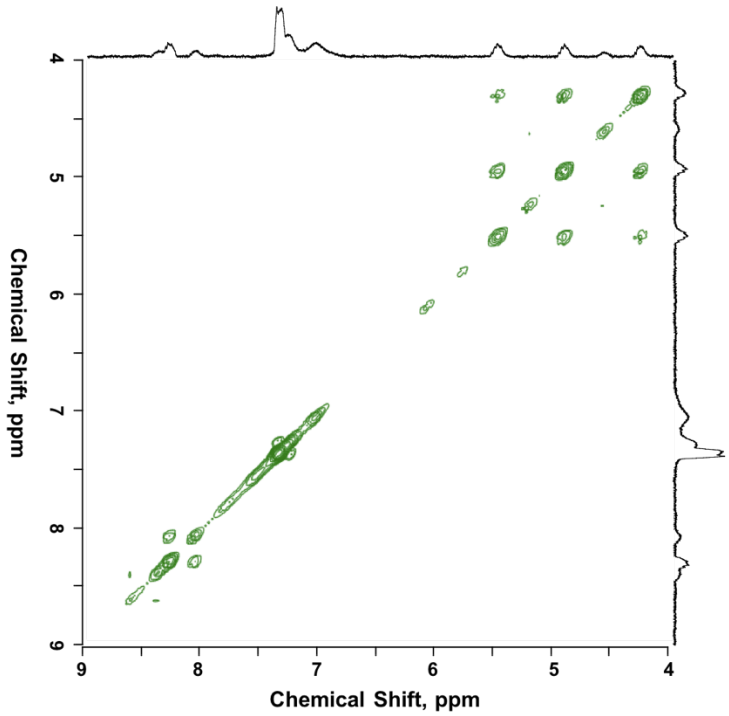

Fig. S19 ^{1}H,^{1}H cosy NMR spectrum of **2Th^{Y}** in the presence of 2 equiv of L^{R} in acetone-d_6 at 298 K.

REFERENCES

(1) B. Li, H. Li, P. Chen, W. Sun, C. Wang, T. Gao, P. Yan, *Dalton Trans*. 2016, **45**, 11459.

(2) B. Li, H. Li, P. Chen, W. Sun, C. Wang, T. Gao, P. Yan, *Phys. Chem. Chem. Phys*. 2015, **17**, 30510.

(3) K. Ono, A. Nakashima, Y. Tsuji, T. Kinoshita, M. Tomura, J. Nishida, Y. Yamashita, *Chem. - Eur. J*. 2010, **16**, 13539.

(4) Y. Yonetoku, H. Kubota, Y. Okamoto, A. Toyoshima, M. Funatsu, J. Ishikawa, M. Takeuchi, M. Ohta, S.-I. Tsukamoto, *Bioorg. Med. Chem.* 2006, **14**, 4750.